COBEM 2021 26th International Congress of Mechanical Engineering
ABCM Associação Brasileira de Engenharia e Ciências Mecânicas
November 22-26, 2021, Virtual Congress, Brazil

COB-2021-0705
A Numerical Study of Rotor Hover Performance at Low Reynolds Number Flow.

Gabrieli Istauro Boni
gabrieli.boni@unesp.br
Daniel Sampaio Souza
daniel.s.souza@unesp.br
Carlos do Carmo Pagani Júnior
c.pagani@unesp.br

São Paulo State University (UNESP). Campus of São João da Boa Vista. Av. Profa. Isette Correa Fontão, 505 - Jardim das Flores, São João da Boa Vista - SP, 13876-750.

Abstract. *This paper reports some preliminary results of an ongoing study focused on investigating the hover efficiency of scaled rotors based on the airfoil geometry and design parameters. The induced flow field and aerodynamic loading are obtained from an in-house numerical code that applies the Blade Element Momentum Theory at low-Reynolds numbers flow, for which a laminar separation bubble is prone to occur and harm the airfoil performance. A rotor configuration with experimental data available in the literature was used as reference. The rotor aerodynamic efficiency is quantified in terms of Figure of Merit for the airfoils FX 63-137 and Eppler 387. For each airfoil, the rotor performance is assessed in terms of thrust coefficient, blade twist rate and blade taper ratio. The results clearly show the role played by the airfoil section geometry and design parameters on the rotor performance and establish a room for rotor design optimization in a broad range of flow Reynolds number. At this stage of the study, emphasis is placed on the combined effect of blade twist and taper ratio for each airfoil geometry.*

Keywords: *Rotary wing, rotor performance, airfoil geometry.*

1. INTRODUCTION

Presently, there is an increasing tendency for the use of small vehicles based on fixed or rotary wings for civilian and military applications. Small rotary-wing-based vehicles are designed with a small geometric scale rotor, which in combination with low speeds of flight results in a low Reynolds number flow based on the wing chord within the range of operational conditions (Mueller and Delaurier, 2003). A characteristic of flow at low Reynolds number is the currency of a laminar separation bubble due to the boundary layer separation over some extent of the airfoil upper surface. Overall, the laminar separation bubble increases the effective drag and reduces the airfoil aerodynamic performance (Mueller and Delaurier, 2003; Carmichael, 1981; Winslow *et al.*, 2018). Therefore, understanding the flow behaviour at low Reynolds number and modelling their aerodynamic effects is the key to improve the performance of small scale aerial vehicles.

Whereas the inviscid flow around the airfoil can be approached by conformal mapping, the viscous effects associated with the laminar bubble separation requires the solution of a set of integral boundary layer equations. Computational Fluid Dynamics is a powerful tool to simulate the viscous-inviscid flow field, but it generally requires a high level of computational resources. The software XFOIL is a practical tool for fast and robust analysis for applications in the aeronautical engineering field. The XFOIL formulation applies the inviscid linear-vortex panel method and the Karman-Tsien compressibility correction to simulate the inviscid flow field, whereas the viscous layer is treated by a two-equation lagged dissipation integral method and numerically solved as a nonlinear system of equations by the Newton's method (Drela, 1989). Such a formulation makes the XFOIL code suitable for the analysis of transitional separation bubbles at low Reynolds number airfoil flow.

Unlike fixed wings, rotary wings undergo a spanwise variation of relative flow speed. The Blade Element Momentum Theory (BEMT) geathers the features of the Momentum Theory, conceived for an actuator disk, and the Blade Element Theory for a finite number of blades. Under some simplifying hypothesis, the BEMT can be applied for a rapid and robust analysis of the effects of airfoil geometry and design parameters on the rotor performance (Leishman, 2006).

This paper reports an ongoing study in which the software XFOIL is applied to calculate drag and lift coefficients of selected airfoils at low Reynolds number flow. The drag and lift coefficients are used as a database, to be accessed by an in-house code for the numerical application of the method BEM, through a table look-up strategy with data interpolation. The BEMT code is then applied to obtain flow parameters, such as the radial distributions of induced flow velocity,

induced angle of attack, aerodynamic loads - force and moments, and rotor performance in terms of design parameters under prescribed operational conditions.

The rotor configuration and experimental data presented in Felker and Mckillip (1994) was used as a reference configuration for a first step validation of our in-house code. This rotor is composed of blades with airfoil section NACA-0015 and the experimental data available for its standard configuration fit flow Reynolds number below 250.000. Our numerical results are in good agreement with these experimental data and with numerical data from Hernandez (2017) for the same rotor configuration.

In this study we investigate the influence of the airfoil geometry on a rotor aerodynamic performance operating at low Reynolds number flow. The airfoils FX 63-137 and Eppler 387 Selig *et al.* (1995) were selected for this study. The rotor performance is quantified based on the Figure of Merit, which is a measure of hover efficiency. An ideal rotor, which requires the minimum power to hover, would achieve a Figure of Merit equal to 1. Real rotors have lower Figure of Merit mainly due to skin drag, which depends on the airfoil section and Reynolds number regime (Carmichael, 1981). For reference, the best hover efficiency of rotors based on conventional technologies lies around 80%, which means that 20% of the power supplied to the rotor shaft must be to overcome drag forces. There is also a tradeoff between rotor designs for thrust efficiency and high-speed flight, so that the Figure of Merit as a measure of rotor performance is here applied to hovering flight.

For each airfoil geometry, the rotor performance is assessed within a range of rotor blades taper ratio and twist radial distribution. Results show the rotor performance is sensitive to each parameter assessed and the highest rotor performance was obtained for the Eppler 387 airfoil at a certain combination of twist angle and taper ratio.

2. METHODOLOGY AND PRELIMINARY DISCUSSION

The performances of rotors with distinguished designs should be evaluated at the same thrust coefficient to allow for a reliable comparison among rotors with distinctive design parameters Leishman (2006), as well as the investigation of the role played by each design parameter, or even a combination of them, to the overall rotor performance. In this study, the thrust coefficient is an entry parameter for numerical simulations of induced flow velocity, aerodynamic load and rotor performance. A numerical iterative scheme is used for tuning the blade pitch angle to the required thrust coefficient at each rotor geometrical configuration and operational condition. Thus, a rotor with a particular airfoil geometry and blade design should be set to a specific blade pitch angle in order to operate at a required thrust coefficient.

A tip loss correction proposed by Prandtl was applied to each rotor blade to account for the three-dimensional flow effect induced by tip vortex. The three-dimensional flow effect at the blade tip region increases the induced flow velocity and reduces lift, and should be considered for more realistic simulations of the rotor blade aerodynamics. Results obtained from our in-house BEM code were compared with experimental thrust and pressure coefficients reported by Felker and Mckillip (1994) for a small-scale rotor tested at the Princeton Long Track Facility, with good agreement between experimental and numerical results. Therefore, the rotor configuration used in this study is closely based on that tested by these authors.

At the rotor operational conditions set for the numerical simulations, all blade sections along the blade span operate at low Reynolds numbers ranging from approximately 50.000 at the blade root to 250.000 at the blade tip. It is well known that, for Reynolds numbers below 10^6, the drag and lift coefficients vary with Reynolds number for most airfoil sections (see for instance Winslow *et al.* (2018)). Further, the assumption of a linear variation of the lift coefficient with angle of attack is generally not valid for Reynolds numbers below 10^6.

In order to achieve realistic flow characteristics at each blade section, a table look-up scheme, with data interpolation, was adopted to estimate the lift and drag coefficients at each blade element in terms of the local effective angle of attack and flow Reynolds number. To accomplish this, the software XFOIL was used to simulate both lift and drag coefficients within a range of angles of attack from -12° to 12° for several Reynolds numbers below 10^6.

Once the numerical results were consistent with experimental data obtained with the airfoil NACA-0015 by Felker and Mckillip (1994), the study was extended to account for the airfoils FX 63-137 (FX Wortmann airfoil) and Eppler 387 (Benchmark Eppler Airfoil), which are airfoils designed for low Reynolds number applications. Figure 1 shows the geometries of the FX 63-137 and Eppler 387 airfoils.

Figure 2 shows the distributions of lift coefficients, (C_l), drag coefficients, (C_d) and the C_l/C_d ratio with the angle of attack, AoA, for the Eppler 387 (E387) and FX 63-137 airfoils. The numerical data shown in Fig. 2 were obtained from simulations with the software XFOIL at Reynolds numbers of 1×10^5, 2×10^5 and 3×10^5, and are part of the database applied in this work to the calculation of the rotor performance. For both airfoils, the results show an approximately linear variation of lift coefficients, except for the highest (negative and positive) angles of attack simulated. The drag coefficients show a low level plateau at low positive angles of attack, which results in a high level of lift-to-drag ratio that peaks around 5°. The low level of the drag coefficients may be associated with laminar flow over most of the airfoil upper surface at the range of lower angles of attack, as well as the increase in the drag coefficient may be associated with the laminar-to-turbulent flow transition at angles of attack higher than 5°. However, these assumptions are not supported by numerical simulations in this work. It is noteworthy the decrease in the C_l/C_d ratio with Reynolds number, which

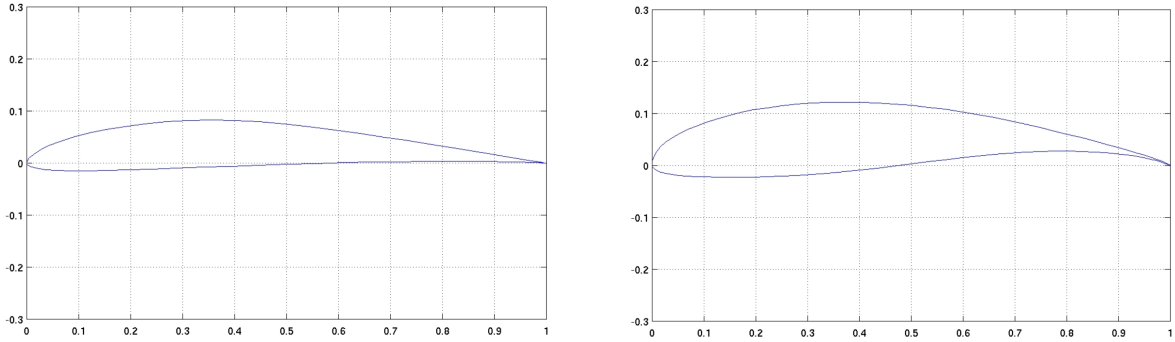

(a) E387 (b) FX 63-137

Figure 1. Eppler 387 and FX 63-137 geometries drawn from the XFOIL software.

possibly occurs due to the increase of pressure drag associated with the enhancement of the separation bubble. Numerical simulations with XFOIL (not shown here) were carried out by using the geometrical coordinates of the model Eppler 387 (A) presented in Selig *et al.* (1995), and the results were compared with experimental data from the same author. Overall, the C_l and C_d coefficients simulated with XFOIL were consistent with experimental data, but the C_l/C_d ratio obtained with Selig's geometry is lower than that shown here. Finally, it is important to note that rotary wings comprise a radial distribution of angles of attack and Reynolds number, so the angle of attack that maximizes the C_l/C_d ratio may occur at a limited length of blade span.

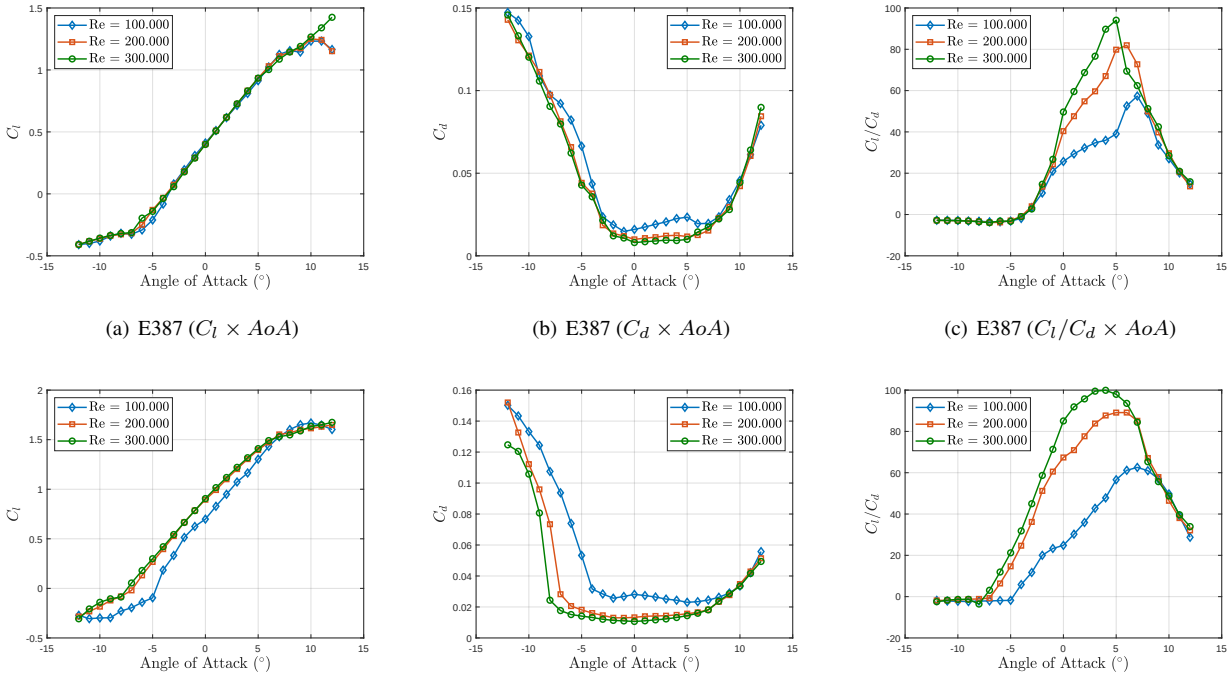

(a) E387 ($C_l \times AoA$) (b) E387 ($C_d \times AoA$) (c) E387 ($C_l/C_d \times AoA$)

(d) FX 63-137 ($C_l \times AoA$) (e) FX 63-137 ($C_d \times AoA$) (f) FX 63-137 ($C_l/C_d \times AoA$)

Figure 2. Distribution of lift and drag coefficients and (C_l/C_d) ratio for the Eppler 387 and FX 63-137 airfoils at Reynolds numbers of 1×10^5, 2×10^5 and 3×10^5.

The laminar separation bubble is expected to occur in both these airfoils' upper surface, which renders them of interest for theoretical studies relating the rotor global performance to the flow field characteristics at low Reynolds number. Due to its larger camber, the FX Wortmann airfoil produces higher lift than the Eppler airfoil for the same angle of attack. It is worth to note that, since both airfoils operate with the same thrust coefficient, the airfoil producing lower lift must operate at a higher effective angle of attack to attain the prescribed thrust coefficient. For this study, the effective angle of attack should be limited to prevent stall and to fall within the range of angles of attack simulated with XFOIL.

A full-scale rotor operating at high Reynolds number was also numerically simulated to serve as a reference for results

from small-scale rotors. Such simulations assumed incompressible flow and spanwise uniform lift coefficient slope of 2π per radian, as predicted by the thin airfoil theory Leishman (2006). The following second order polynomial equation was used to represent the drag coefficient in terms of the effective angle of attack, α,

$$C_d(\alpha) = 0,01 + 0,025\alpha + 0,65\alpha^2, \tag{1}$$

in which the numerical coefficients were empirically determined for full-scale helicopter airfoils (Leishman, 2006; Bohorquez, 2007).

The effective angle of attack is defined by

$$\alpha = \theta - \phi, \tag{2}$$

where θ is a geometric angle of attack comprised by the blade pitch angle and the radial distribution of twist angle, and ϕ is the angle of attack induced by the flow field normal to the rotor plane, also known as induced angle of attack. The radial distributions of induced flow velocity and angle of attack depend on rotor and blade parameters design and play an important whole on the rotor induced power and aerodynamic performance.

In this study, the rotor performance is represented by the Figure of Merit, which is defined by the ratio between the ideal induced power and the real power required to hover the rotor at a given operational condition,

$$FM = \frac{Ideal\ Power}{Induced\ Power\ +\ Profile\ Power} = \frac{C_T^{3/2}/\sqrt{2}}{C_{P_i} + C_{P_o}}. \tag{3}$$

In Eq. 3, C_T is the thrust coefficient, C_{P_i} is the induced power and C_{P_o} is the profile power. The induced power is the power required to generate lift from the induced flow and the profile power accounts for viscous effects such as skin friction, flow separation and pressure drag.

The numerical implementation of the *Blade Element Momentum* was based on Leishman (2006). Each blade was discretized in a number N of 100 elements, which was enough to ensure a good approximation of an uniform flow through each blade element and render the results independent of the blade discretization. Induced and profile power coefficients were obtained by numerical integration along the blade span as follows:

$$C_{P_i} = \sum_{n=1}^{N} \Delta C_{T_n} \lambda_n, \quad C_{p_o} = \frac{1}{2} \sum_{n=1}^{N} \sigma_n C_{d_0} \bar{r}_n^3 \Delta \bar{r}_n. \tag{4}$$

In Eq. 4, λ_n is the nondimensional induced flow velocity, which is a function of the radial position, $\bar{r}_n$, and the lift coefficient slope, C_{l_α}, which for low Reynolds number simulation is also a function of $\bar{r}_n$. Here, the superscript bar symbol indicates nondimensional radial position, obtained by dividing the radial position by the blade length, so that $0 \leq \bar{r} \leq 1$. For each blade section along the blade span, the lift coefficient slope is obtained based on the local angle of attack and Reynolds number, by inspecting a look-up table. To render the numerical approach fully consistent with the hypothesis of a spanwise constant lift coefficient slope assumed in the calculation of a thrust-weighted solidity, a mean lift coefficient slope is obtained by averaging the local quantities across the blade span. The drag coefficient, C_{d_0} is also obtained from a look-up table scheme.

2.1 Blade Tapering Based on Thrust-Weighted Solidity

Consider a linearly-tapered wing with local solidity $\sigma(\bar{r})$, which generates a spanwise constant lift coefficient, $\bar{C}_l$. The thrust coefficient for such a blade is given by:

$$C_T = \frac{\bar{C}_l}{2} \int_0^1 \sigma(\bar{r})\, \bar{r}^2 d\bar{r}. \tag{5}$$

A rectangular blade with equivalent solidity, σ_e, which produces the same thrust coefficient as a tapered blade, is given in terms of σ_e and $\bar{C}_l$ as follows

$$C_T = \frac{\sigma_e}{2} \bar{C}_l \int_0^1 \bar{r}^2 dr = \frac{\sigma_e}{2} \bar{C}_l \left[\frac{\bar{r}^3}{3} \right]_0^1 = \frac{\sigma_e}{6} \bar{C}_l \tag{6}$$

By comparing Eqs. 5 e 6, one obtains

$$\sigma_e = 3 \int_0^1 \sigma(\bar{r})\, \bar{r}^2 d\bar{r}. \tag{7}$$

Supposing the following linear variation of $\sigma(\bar{r})$ with $\bar{r}$

$$\sigma(\bar{r}) = \sigma_0 + \sigma_1 \bar{r}, \tag{8}$$

Equation 7 leads to

$$\sigma_e = 3\int_0^1 [\sigma_0 + \sigma_1 \bar{r}]\, \bar{r}^2 d\bar{r} = \sigma_0 + \frac{3}{4}\sigma_1. \tag{9}$$

Now, it turns out that

$$\sigma(\bar{r} = 0,75) = \sigma_0 + \frac{3}{4}\sigma_1. \tag{10}$$

Therefore, a rectangular blade whose solidity matches the local solidity of a tapered blade at $\bar{r} = 0,75$ produces the same lift as the tapered blade. Fig. 3 (a) shows a linearly tapered blade of length R, root-chord denoted by c_{root}, and tip-chord denoted by c_{tip}, along with a rectangular blade of constant equivalent chord c_e.

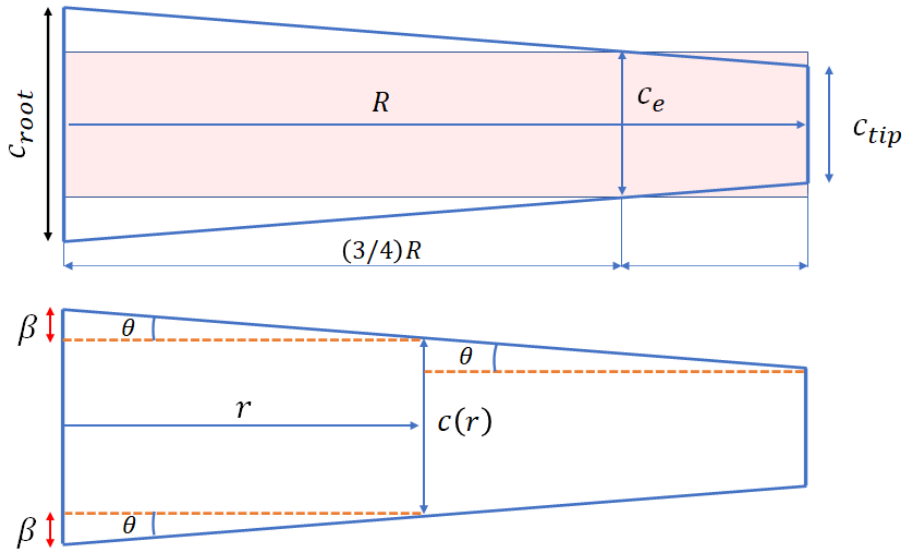

(a)

Figure 3. Sketch of (a) tapered blade and rectangular (colored) blade with thrust-weighted equivalent chord, (b) basic geometric considerations to calculate the local solidity of a blade with taper ratio γ.

Once the equality $c_{root} = \gamma c_{tip}$ holds for a blade with linear taper ratio γ, from Fig. 3 (b), the chord length at an arbitrary radial position is given by

$$c(\bar{r}) = \gamma c_{tip} - 2\beta. \tag{11}$$

To take into account the blade parameters design, we can calculate $\tan\theta$ by considering the whole length of the blade, so that

$$\tan\theta = \frac{c_{root} - c_{tip}}{2R} = \frac{\gamma c_{tip} - c_{tip}}{2R} = \left(\frac{\gamma - 1}{2R}\right) c_{tip}. \tag{12}$$

By taking $\beta = r\tan\theta$, the chord length is given by

$$c(\bar{r}) = \gamma c_{tip} - 2r\left(\frac{\gamma - 1}{2R}\right) c_{tip}. \tag{13}$$

By simple algebraic manipulation, with $\bar{r} = r/R$, the chord length writes

$$c(\bar{r}) = \gamma c_{tip} - \bar{r}\gamma c_{tip} + \bar{r} c_{tip} = [(1-\gamma)\bar{r} + \gamma]\, c_{tip}. \tag{14}$$

However, for a thrust-weighted solidity, the equivalent chord of a rectangular blade must correspond to the local chord length of a tapered wing at $\bar{r} = 0,75$ ($c_e = c(\bar{r} = 0,75)$), so that a relationship between c_e and c_{tip} can be obtained by evaluating Eq. 14 at $\bar{r} = 0,75$

$$c_e = [(1-\gamma)\,0,75 + \gamma]\,c_{tip}, \tag{15}$$

from which one obtains c_{tip} in termos of the equivalente chord, c_e:

$$c_{tip} = \frac{c_e}{(1-\gamma)\,0,75 + \gamma}. \tag{16}$$

By inserting Eq. 16 into Eq. 14 we obtain $c(\bar{r})$ in terms of c_e, as follows

$$c(\bar{r}) = \frac{(1-\gamma)\,\bar{r} + \gamma}{(1-\gamma)\,0,75 + \gamma} c_e. \tag{17}$$

The local solidity of a rotor with N_b non-rectangular blades having variable chord length is defined by

$$\sigma(\bar{r}) = \frac{N_b c(\bar{r})\,\bar{r}}{\pi \bar{r}^2} = \frac{N_b c(\bar{r})}{\pi \bar{r}}, \tag{18}$$

whereas the equivalent local solidity of a rectangular blade is defined by

$$\sigma_e = \frac{N_b}{\pi \bar{r}} c_e. \tag{19}$$

By using the relationship between chord length and solidity defined in Eqs. 18 and 19, it is a simple task to recast Eq. 17 in terms of local and equivalent solidities

$$\sigma(\bar{r}) = \frac{(1-\gamma)\,\bar{r} + \gamma}{(1-\gamma)\,0,75 + \gamma} \sigma_e. \tag{20}$$

Since the equivalent solidity is an entry parameter for simulating the rotor performance, Eq. 20 was applied in this study to calculate the local rotor solidity for linearly tapered blades, with $\gamma = 1$, $\gamma = 2$ and $\gamma = 3$ designating rectangular blade and blades with taper ratios of 2:1 and 3:1, respectively. The rigorous application of the concept of thrust-weighted solidity requires the same lift coefficient distribution among the rotors compared. Therefore, this concept is applied here as an approximation to assess the effect of the linear tapper on the aerodynamic performance of rotors with the same airfoil geometry.

3. RESULTS AND DISCUSSION

In this section, the rotor Figure of Merit is presented as a function of the thrust coefficient, wing taper ratio and radial twist distribution for the FX 63-137 and Eppler 387 airfoils. Results from a generic airfoil simulated at high Reynolds number are also presented for reference. To better understand the influence of each simulation parameter on the flow around the wing, we first investigate the effect of the airfoil section geometry, blade root-to-tip linear taper ratio and linear twist rate on the radial distribution of the effective wing angle of attack. The rotor blades are 1.22 m in length. A rotor solidity of 0.10 was adopted for rectangular and tapered (equivalent solidity) blades.

Figure 4 shows the radial distribution of the effective wing angles of attack of a rotor with four rectangular blades (taper ratio of 1:1) operating at thrust coefficients ranging from to 0.0020 to 0.01, in step of 0.0005. The blades were simulated with -10° root-to-tip linear twist rate. In the calculation of the effective angle of attack with the Blade Element Momentum code, the pitch angle varies with the airfoil geometry to achieve a prescribed thrust coefficient, whereas the induced angle of attack is related to the spanwise distribution of the induced velocity.

According to the results shown in Fig. 4, the angle of attack increases with the thrust coefficient for each airfoil section geometry. The highest lift produced by the generic airfoil induces the lowest effective angles of attack, whereas the smaller lift produced by the Eppler 387 airfoil induces the highest ones. For each airfoil geometry and thrust coefficient, the highest angle of attack occurs at the inbord regions of the wings.

Figure 5 shows the radial distribution of the effective wing angles of attack for the same four-bladed rotor configuration, simulated with thrust coefficient of 0.008 and twist angle varying from 0 to -35°, with step of -5°. For an untwisted blade, the highest angle of attack occurs near the wing tip. However, a twist rate of -15° is enough to shift the spanwise region of highest angle of attack to the inboard of the wing. From the inboard region toward the tip, the angle of attack continuously decreases up to small values for high twist rates at the blade tip. The highest the twist angle, the highest the angle of attack and the steepest the rate of decrease toward the tip. Such a trend is verified for all airfoils tested, but the airfoil geometry mainly impacts on the value of the angle of attack in the inboard region of the wing.

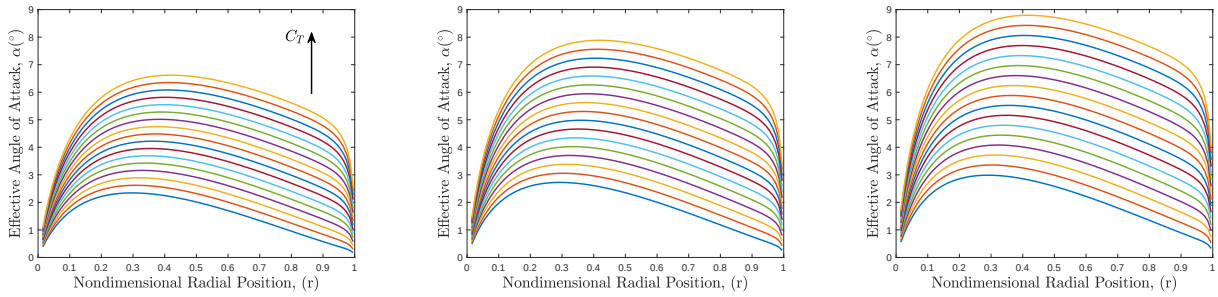

(a) Generic airfoil (b) FX 63-137 airfoil (c) Eppler 387 airfoil

Figure 4. Radial distributions of angle of attack as a function of thrust coefficient: 4(a) generic airfoil, 4(b) FX 63-137 airfoil e 4(c) Eppler 387 airfoil. The angle of attack increases with C_T.

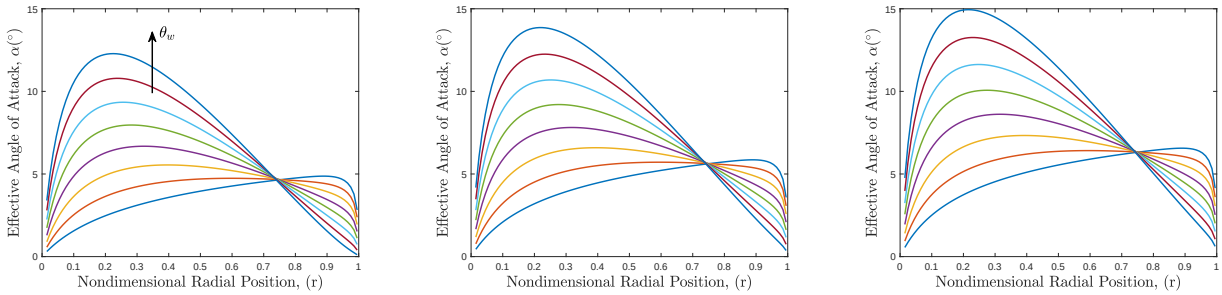

(a) Generic airfoil (b) FX 63-137 airfoil (c) Eppler 387 airfoil

Figure 5. Radial distributions of angle of attack as a function of linear twist rate: 5(a) generic airfoil, 5(b) FX 63-137 airfoil e 5(c) Eppler 387 airfoil. The angle of attack increases with the twist angle, θ_w.

Figure 6, in turn, shows the effect of a linear taper distribution on the effective angle of attack for a rotor with four untwisted blades simulated with thrust coefficient of 0.008. According to the results, the rectangular profile produced higher angles of attack in the inboard region of the wing, whereas the tapered wings increased the flow uniformity along most of the blade span. Such an uniform flow distribution is also observed in Fig. 5 for a twist rate of -10°. However, according to our simulations, an uniform angle of attack is not, in general, associated with an uniform induced flow across the blade span, although taper ratio and twist rate can be trim to approach the induced flow to the ideal uniform inflow, thus minimizing the induced power and improving the rotor aerodynamic efficiency. It is also noteworthy the case in which an uniform angle of attack can be approached to the angle for the best airfoil lift-to-drag ratio. Finally, when comparing the airfoil sections geometry, the highest angle of attack was found for the Eppler 387 airfoil.

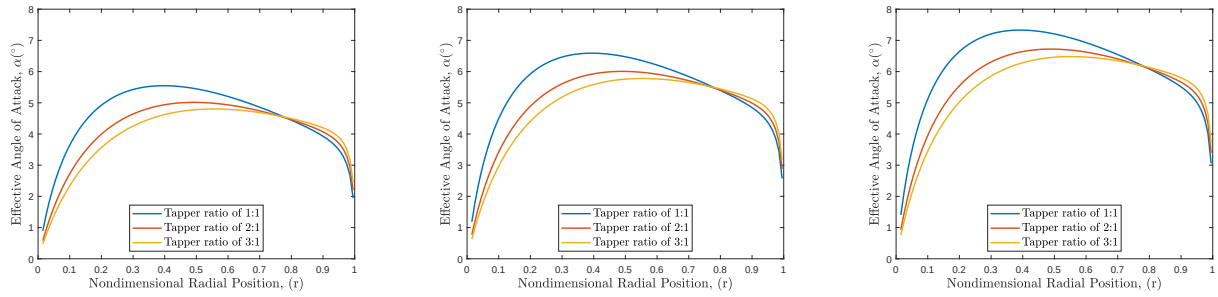

(a) Generic airfoil (b) FX 63-137 airfoil (c) Eppler 387 airfoil

Figure 6. Radial distributions of angle of attack as a function of blade taper ratio: 6(a) generic airfoil, 6(b) FX 63-137 airfoil e 6(c) Eppler 387 airfoil.

Figure 7 shows the Figure of Merit as a function of the thrust coefficient for blades with rectangular planform and taper

ratios of 2:1 and 3:1. For the airfoil geometries simulated, the Figure of Merit increases with the thrust coefficient and seems to reach a plateau from $C_T = 0.01$. The Generic and FX 63-137 airfoils show similar aerodynamic performance, whereas the airfoil Eppler 387 presents higher Figure of Merits at lower thrust coefficients, followed by a tendency of decrease beyond $C_T = 0.009$. Overall, there is a tendency of increase in the Figure of Merit with the blade taper ratio.

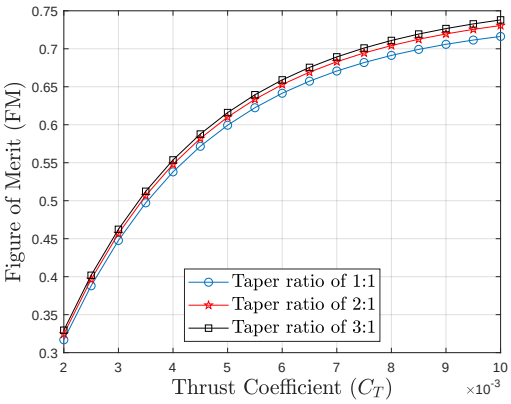

(a) Generic Airfoil.

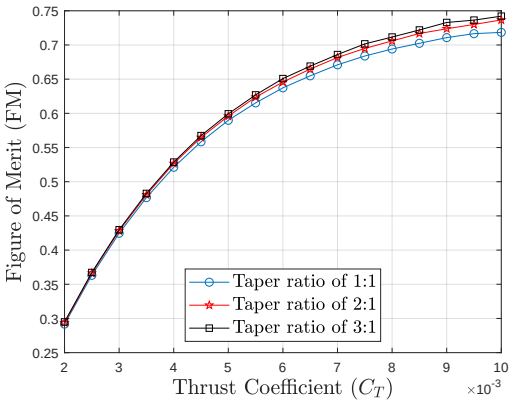

(b) FX 63-137 airfoil

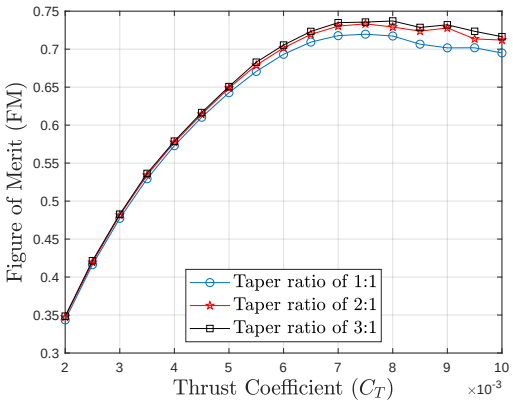

(c) Eppler 387 airfoil

Figure 7. Figure of Merit as a function of the thrust coefficient for three airfoil sections.

In Figure 8 we present results of simulations combining the effects of the blade taper ratio and twist angle on the rotor performance. Blade taper ratios of 1:1 (rectangular blade), 2:1 and 3:1 were adopted in this study and for each taper ratio the blade twist angle ranged from 0° to -35°, with step of -5°. The thrust coefficient was set to 0.008. The concept of equivalent thrust coefficient is applied, so that rotors with blades of different taper ratios are designed to operate at the same thrust condition, which is achieved by designing rotors with same thrust-weighted solidity. Such an approach allows for evaluating the net effect of the blade taper ratio on the rotor performance.

For the generic and FX 63-137 airfoils, the relevant increase in the Figure of Merit with taper ratio occurs in the range of low to intermediate twist angles, reaching the maximum around -15° for taper ratio of 3:1. For the Eppler 387 airfoil, the relevant effect of the wing taper ratio on the Figure of Merit is observed in the range of intermediate twist angles, where an increase of around 2.6% is observed by comparing results for taper ratios of 1:1 and 2:1 at twist angle of -15°. The airfoil Eppler 387 with taper ration of 3:1 reached the maximum Figure of Merit of 0.75 at twist angle of -10°, and showed effects of the taper ratio more pronounced at higher twist angles, when compared with the generic and FX 63-137 airfoils.

4. CONCLUSION

This paper presents preliminary results from an ongoing study to investigate the flow features and rotor performance at low Reynolds number flow. Numerical simulations of small-scale rotors based on the Blade Element Momentum Theory were carried out to obtain the rotor performance based on design parameters using the FX 63-137 and Eppler 387

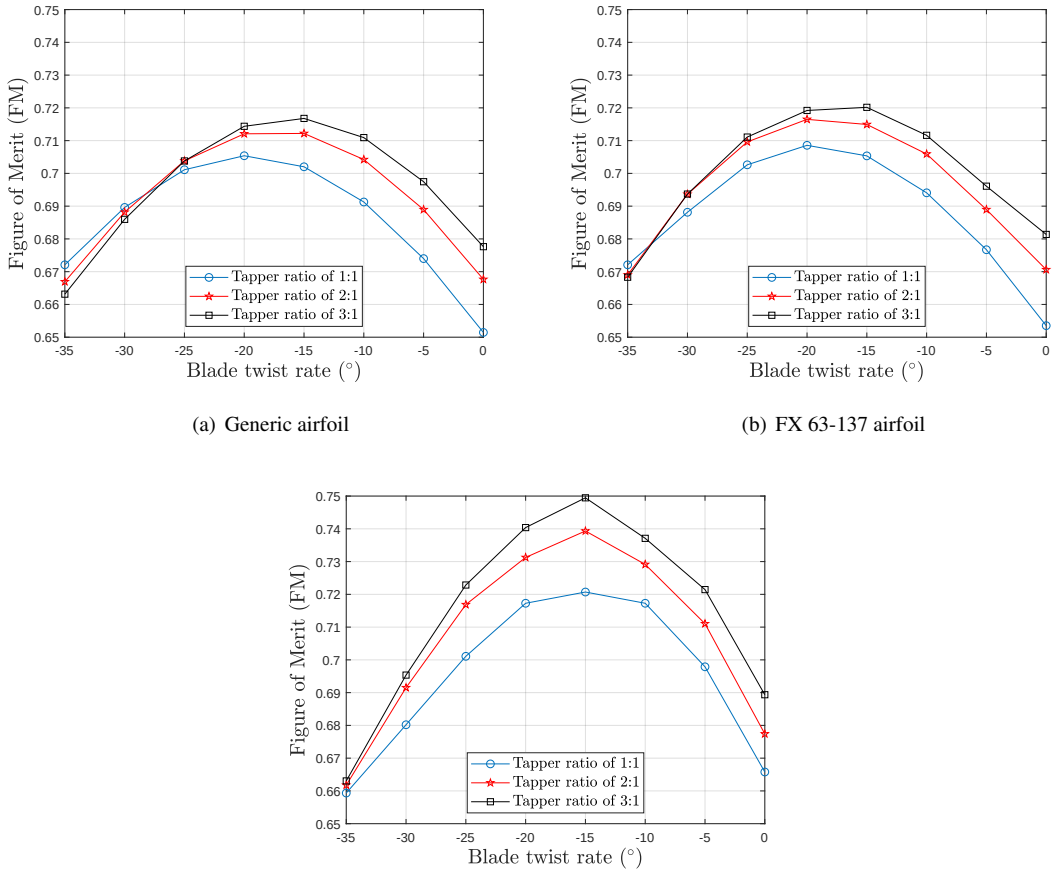

(a) Generic airfoil

(b) FX 63-137 airfoil

(c) Eppler 387 airfoil

Figure 8. Figure of Merit as a function of the blade twist rate and tapper ratio for three airfoil sections.

airfoils. The rotor performance for each airfoil section was assessed within a selected range of thrust coefficients, taper ratio and twist angle distribution. The Blade Element Momentum method was able to identify the role played by each design parameter and airfoil section geometry on the rotor performance based on a metric of efficiency called Figure of Merit. The results show the airfoil performance under low Reynolds number flow can be strongly dependent on designing parameters and operational conditions. The preliminary achievements support further studies focused on optimizing the performance of rotors operating at low Reynolds number flow.

5. ACKNOWLEDGEMENTS

The first author acknowledges the support received from State of São Paulo Research Foundation (Proc. 2020/06666-4). The last author is grateful to Prof. J. Gordon Leishman for his valuable support on the Blade Element Momentum Theory at the initial stage of this work.

6. REFERENCES

Bohorquez, F., 2007. *Rotor Hover Performance and System Design of an Efficient Coaxial Rotary Wing Micro Air Vehicle*. Ph.D. thesis, Department of Engineering of University of Maryland, College Park, MD 20742, EUA.

Carmichael, B.H., 1981. "Low reynolds number airfoil survey. volume 1, nasa contractor report ID 165803, https://ntrs.nasa.gov/citations/19820006186. accessed 20 june 2021".

Drela, M., 1989. *XFOIL: An Analysis and Design System for Low Reynolds Number Airfoils*. Springer, Berlin, Heidelberg.

Felker, F.F. and Mckillip, R.M., 1994. "Comparisons of predicted and measured rotor performance in vertical climb and descent". *50th Annual Forum of the American Helicopter Soc., Washington DC, May 11-13*.

Hernandez, J.L.L., 2017. *Verification of a Modelica Helicopter Rotor Model Using Blade Element Theory*. Ph.D. thesis, Department of Management and Engineering of Linköping University, Link ö ping, Sweden.

Leishman, J.G., 2006. *Principles of Helicopter Aerodynamics 2nd edn*. Cambridge Univeristy Press, New York.

Mueller, T.J. and Delaurier, J.D., 2003. "Aerdynamics of small veiches". *Annual Review of Fluid Mechanics*, Vol. 35, No. 1, pp. 89–111.

Selig, M.S., Guglielmo, J.J., Broeren, A.P. and Giguère, P., 1995. "Summary of low-speed airfoil data". *SoarTech Publications, Virginia Beach, Virginia*, Vol. 1.

Winslow, J., Otsuka, J., Govindarajan, H. and Chopra, B., 2018. "Basic understanding of airfoil characteristics at low reynolds numbers". *Journal of Aircraft*, Vol. 33, pp. 1015–1061.

7. RESPONSIBILITY NOTICE

The authors are solely responsible for the printed material included in this paper.